Engineering Fracture Mechanics 228 (2020) 106889

Contents lists available at ScienceDirect

Engineering Fracture Mechanics

journal homepage: www.elsevier.com/locate/engfracmech

HOTPITS: The DARWIN approach to assessing risk of hot corrosion-induced fracture in gas turbine components

K.S. Chan[a,*], M.P. Enright[a], J. Moody[a], C. Thomas[b], W. Goodrum[b]

[a] Southwest Research Institute, San Antonio, TX 78238, USA
[b] Elder Research Inc., Charlottesville, VA 22901, USA

ARTICLE INFO

Keywords:
Hot corrosion
Pit nucleation and growth
Pit coalescence
Pit-to-crack transition
Probabilistic life prediction

ABSTRACT

HOTPITS is a set of physics-based software tools for treating the degradation processes in Type II hot corrosion, including the initiation, growth, and coalescence of multiple pits, and the transition of pits to fatigue cracks. The HOTPITS methodology has been implemented in DARWIN® to provide a probabilistic capability for assessing the risk of hot corrosion-induced fracture in gas turbine components. To illustrate model capabilities, two benchmark computations were performed to simulate the initiation, growth, and coalescence of multiple pits, and their transition to a dominant Mode I crack and to assess the risk of hot corrosion–induced fracture.

1. Introduction

Hot corrosion is a concern in advanced gas engine component because of higher service temperatures [1–10] and the potential use of low-grade fuels or biomass-derived fuels with relatively high sodium, sulfur, and chloride contents [11]. Hot corrosion can be more severe in aircraft engines that are used in coastal areas, over deserts, and volcanic regions where high chloride bearing salts and fine sulfate bearing sands can be ingested in the engines [12]. Under sponsorship by NASA, Elder Research Inc. (ERI) and Southwest Research Institute (SwRI) have developed a set of physics-based modeling tools to predict hot corrosion in Ni-based super-alloys [13]. These modeling tools are capable of predicting the formation, growth, and coalescence of hot corrosion pits, as well as transition of pits to microcracks, and the propagation of the microcracks to failure. These analysis tools have been implemented into a commercial probabilistic life-prediction code called DARWIN [14] to enhance the current capability to simulate and avoid corrosion fatigue failure of engine disks and metallic structural components due to prolonged exposures to extreme environments at elevated temperatures, and to assess the reliability of advanced gas turbine engines.

The objective of this investigation is the development of a set of physics-based modeling tools for predicting and mitigating the onset of Type II hot corrosion in advanced Ni-based superalloys. The salient characteristics of Type II hot corrosion include the formation of corrosion pits that subsequently induce fatigue crack formation and growth [5–8]. From a damage tolerance viewpoint, localized attack by a self-sustaining corrosion mechanism is more dangerous as it would typically lead to high stress concentration and fatigue crack formation at the pits [15]. In an earlier paper [16], Type II hot corrosion is modeled as a process that involves the deposition of sulfates on metal surface and the formation of corrosion pits on the metal surface due to localized attacks on the protective oxide scales by corrosive gases such as SO_3. A set of hot corrosion models will be presented for treating the deposition of alkali sulfates, the initiation and the growth of pits, and the transition of pits to cracks during Type II hot corrosion. This set of hot corrosion models has been implemented and utilized in conjunction with a probabilistic life-prediction code, called DARWIN [14], to

* Corresponding author at: MESI Technologies LLC, San Antonio, TX 78250, USA.
E-mail address: kchansatx@icloud.com (K.S. Chan).

https://doi.org/10.1016/j.engfracmech.2020.106889
Received 27 September 2019; Received in revised form 12 January 2020; Accepted 13 January 2020
Available online 23 January 2020
0013-7944/

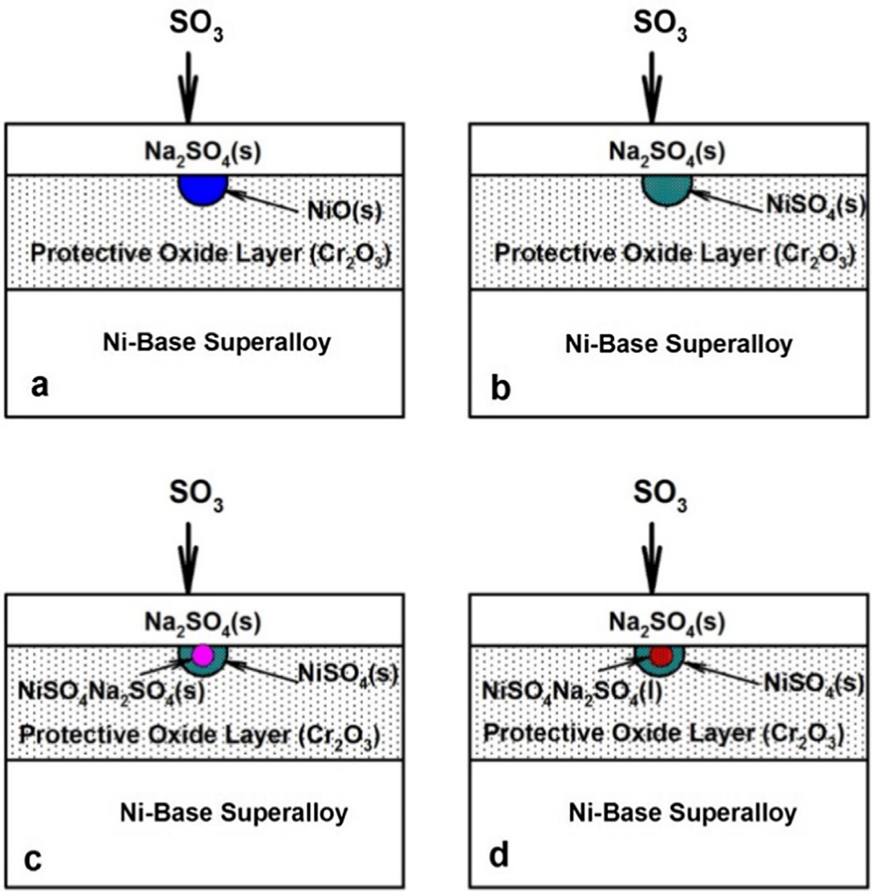

Fig. 1. Schematics of Type II hot corrosion envisioned in the development of the pit initiation model: (a) formation of NiO in the protective oxide (Cr_2O_3) layer formed on a Ni-based superalloy, (b) reaction of NiO with SO_3 to form $NiSO_4$, (c) interaction of $NiSO_4$ with Na_2SO_4 to form a solid $NiSO_4{\cdot}Na_2SO_4$ particle, and (d) solid $NiSO_4{\cdot}Na_2SO_4$ becomes molten as the composition approaches the eutectic composition. From Chan et al. [16].

enable assessment of the risk of hot corrosion-induced failure in gas turbine disks. Benchmark computations have been performed to illustrate the initiation and growth of a single hot corrosion pit, the transition of a single pit to a single crack, and the subsequent propagation of the dominant fatigue crack to disk failure [15,16].

In this article, we report of the results of the efforts to extend the single-pit models [15,16] to treat the nucleation, growth, and coalescence of multiple pits occurring at different temperatures, times, and locations of a gas turbine disk. The coalesced pits are allowed to evolve to become microcracks. After their formation, the microcracks are allowed to grow and coalesce to form larger cracks, until a dominant crack forms and propagates to fracture. This probabilistic methodology of treating the nucleation, growth, and coalescence of hot corrosion pits and microcracks is named HOTPITS. This is the second of a series of three papers on the HOTPITS methodology. In the first part [16], the formulation of the various models on sulfate deposition, pit nucleation, and pit growth were presented and applied to treat the damage process involving the nucleation and growth of a single pit to become a single large crack. In this articles, we report the methodology for treating a hot corrosion process involving the nucleation, growth, and coalescence of multiple pits and microcracks in a gas turbine disk. In the third paper [17], validation results of the HOTPITS methodology are evaluated and assessed against critical laboratory experiments.

2. HOTPITS methodology

Type II hot corrosion can be separated into initiation and propagation stages [3]. During the initiation stage, the corrosion rate is comparatively low as the breakdown of the protective oxide occurs. Once the breakdown of the protective oxide has occurred, the propagation phase commences and produces a rapid metal loss since repair or recovery of the protective oxide scale is no longer possible. The initiation phase of hot corrosion has been modeled by considering that the sulfate liquid layer from the cooler metal surface solidifies rapidly into a solid sulfate phase instantly. Furthermore, the metal surface, which is either a Ni-based or a Co-based superalloy, is stipulated to form a protective oxide scale, as depicted in Fig. 1(a). The protective oxide scale, however, contains small amounts of NiO within the protective oxide layer. It is envisioned that the sulfur impurities in the fuels results in the formation of SO_2 and SO_3, which diffuse through the sulfate layer on the metal surface and react with NiO in the oxide layer to form $NiSO_4$ in the solid

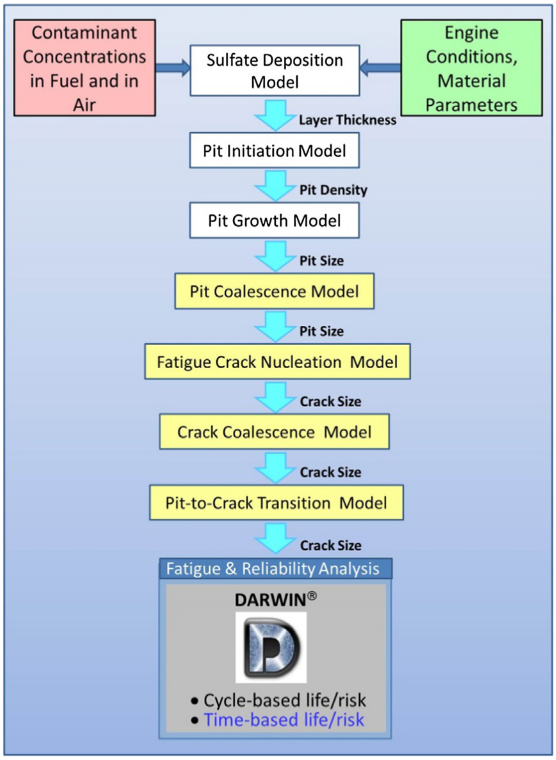

Fig. 2. Schematics of the hot corrosion prediction methodology.

form, Fig. 1(b). When $NiSO_4$ in the oxide layer and the Na_2SO_4 in the sulfate layer come into contact with each other, they react to form a $NiSO_4 \cdot Na_2SO_4$ ($NiNa_2(SO_4)_2$) complex with a low melting point [9,18,19]. The sulfate complex is initially formed as a solid, as depicted in Fig. 1(c), but it becomes a liquid when the composition of sulfate complex approaches the eutectic composition, Fig. 1(d). In liquid form, the sulfate complex is corrosive and can dissolve or crack the protective layer (e.g., Cr_2O_3) [1–3,7–9], thereby reducing the effectiveness of the protective oxide scale. The initiation of hot corrosion is considered to commence when the $NiNa_2(SO_4)_2$ becomes a liquid phase and the molten liquid attacks the protective oxide layer beneath the sulfate layer by dissolving the protective oxide scale.

To address Type II hot corrosion, a physics-based hot corrosion prediction methodology, dubbed HOTPITS, has been developed according to the schematics outlined in Fig. 2. The key features of the probabilistic framework, shown in Fig. 2, are: (1) a sulfate deposition model for predicting the formation of a sulfate layer on hot-section components based on input from contaminant concentrations in the fuel and in the air as well as relevant engine conditions, (2) a pit initiation model for predicting pit density, and (3) a pit growth model for predicting pit size as a function of time of hot corrosion. These three models, which are shown in boxes with a white background, have been implemented in DARWIN and utilized to simulate the initiation and growth of a single hot corrosion pit and its transition from a microcrack that ultimately propagates to failure. The results of this work were summarized in an earlier publication [16]. In this investigation, the pit initiation and growth models are further extended to treat multiple pits. In addition, a set of criteria has been developed for predicting the onset of active and dormant (non-active) states for hot corrosion. During active states, hot corrosion occurs by the nucleation, growth, and coalescence of hot-corrosion pits. During dormant or non-active states, progression of hot corrosion ceases to continue but fatigue cracks may nucleate, grow, and coalesce at previously formed hot-corrosion pits. To incorporate these damage processes during Type II hot corrosion, the pit initiation and growth models are also coupled with a pit coalescence model, a fatigue crack nucleation model, a microcrack coalescence model, and an enhanced pit-to-crack transition model. These advanced pit evolution models involving multiple pits and microcracks are highlighted in boxes with a yellow background (on-line version) in Fig. 2. These algorithms are implemented and are collectively referred to as HOTPITS in the DARWIN probabilistic life-prediction code. Development of these physics-based modeling tools are described in Section 2. Results of model simulations performed to verify the software tools are presented in Section 3, followed by Discussion and Conclusion. Besides verification, these software tools have also been validated by critical experiments and benchmark computations. The results of the validation experiments and benchmark computations are presented in the companion publications [13,17].

In this article, the term 'verification' is used to mean that the values of the mathematical models and software tools have been checked to ensure that the mathematical equations have been implemented correctly and the computed values are correct. In addition, the models reproduce correctly the experimental data or material response for which the models are intended to represent. In contrast, the term 'validation' is used to mean that the predicted model response has been quantitatively compared with good agreement against independent experimental data that have not been used to develop the models or utilized to obtain the model

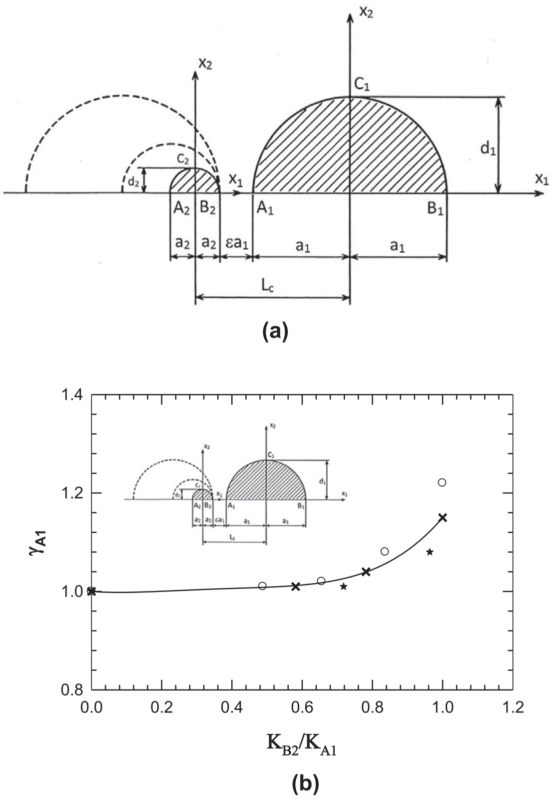

Fig. 3. (a) Schematics of the interaction of two semi-circular microcracks of different surface lengths ($2a_1$ and $2a_2$) and depths (b_1 and b_2) separated by a tip-to-tip spacing of εa_1 and a center-to center spacing of L_c. modified from [20]; (b) Interaction parameter, γ_{A1}, as a function of the ratio of K_{B2} to K_{A1}, where K_{B2} is the stress intensity factor at tip B_2 and K_{A1} is the stress intensity at tip A_1. Values of γ_{A1} are from [20].

constants. On the bases of these definitions, only model verification of the models has been performed in this article. In comparison, validations of the hot corrosion and fatigue models are reported in the companion paper [17] since independent experiments were performed to generate critical data to compare against the relevant models.

3. Modeling tool development

3.1. Coalescence of unequal-sized pits

The coalescence of unequal-sized pits is considered by treating a pair of unequal-sized pits as a pair of unequal-sized semi-spherical microcracks of crack length $2a_i$ and crack depth b_i, as shown in Fig. 3(a), where $i = 1$ or 2. The stress intensity factor (K) solutions for the interactions of a pair of asymmetric microcracks are available from the literature [20] for various crack sizes and center-to-center spacing. For instance, the interaction parameter, γ_{A1}, for the microcrack tip A_1 due to microcrack tip B_2 is presented in Fig. 3(b) as a function of the ratio of the stress intensity factor at tip B_2 to that at tip A_1. The interaction parameter is defined as the ratio of the dimensionless stress intensity factor of the microcracks to that of a single crack subject to the same loading [20]. In general, the value of the interaction parameter, γ_{A1}, increases with increasing K values at the approaching crack tip, B_2. The interaction parameter also depends on the ratio, λ, of the crack size to the center-to-center (L_c) spacing between the two microcracks, where λ is defined as

$$\lambda = \frac{a_1 + a_2}{a_! + a_2 + \varepsilon a_1} \tag{1}$$

where ε is an arbitrary constant, a_1 is the half length of the larger microcrack, and a_2 is the half-length of the smaller microcrack. Fig. 4(a) shows a plot of the interaction parameter, γ_{A1}, as a function of λ for three different values of the ratio of a_2/a_1 (0, 0.5, and 1). It is noted that the value of γ_{A1} increases rapidly when the distance between the microcracks decreases or the normalized crack size parameter λ increases. The two microcracks are of equal size when $a_2/a_1 = 1$. As a special case, the coalescence of two interacting equal-sized pits can be treated as a pair of twin cracks. The normalized stress intensity factors (i.e., boundary-correction factors) at the tips of the surface crack (A and B) and at the crack depth (C) were obtained from the literature [20] as a function of the ratio of crack depth to spacing, λ (=2a/L_c). After reviewing the stress intensity factor solutions for twin cracks, it becomes apparent that the ligament between the twin pits or cracks would be most highly stressed. The interaction is most effective when the two pits are close

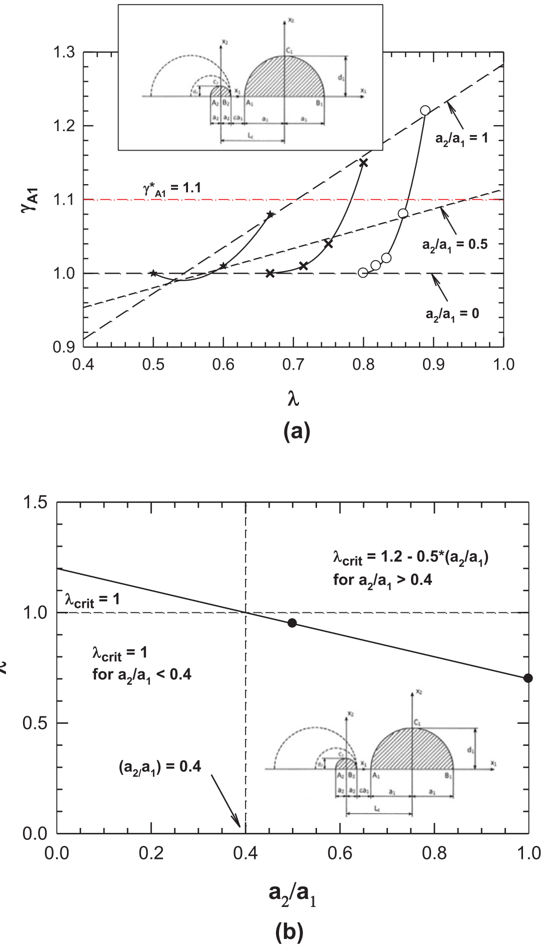

Fig. 4. (a) Interaction parameter, γ_{A1}, as a function of λ for various crack size ratio, a_2/a_1. Values of γ_{A1} are from [20]; (b) the criteria for the coalescence of two unequal-sized microcracks illustrated in a plot of λ versus crack size ratio (a_2/a_1).

to each other with a spacing that is less the $2a$. Thus, the pit spacing is an important parameter that controls the interactions with two or multiple pits. Thus, a critical spacing is utilized as the criterion for pit coalescence in HOTPITS. A critical value of $\lambda = 0.7$ was chosen for the coalescence of two equal-sized microcracks ($a_2/a_1 = 1$). It corresponds to a critical value of $\gamma_{A1} = 1.1$, as indicated by the red dot-dashed line in Fig. 4(a). To achieve the same critical value of γ_{A1} for $a_2/a_1 = 0.5$, the microcrack spacing needs to be as high as 0.95, as shown in Fig. 4(a). These results were utilized to establish a coalescence criterion for unequal-sized microcracks (or pits) in Fig. 4(b), which indicates that compared to two equal-sized microcracks, two unequal-sized microcracks need to come closer together before coalescence can take place. For $a_2/a_1 > 0.4$, coalescence of two unequal-sized microcracks take place when

$$\lambda_{crit} = 1.2 - 0.5 * (a_2/a_1) \tag{2}$$

and

$$\lambda_{crit} = 1 \tag{3}$$

when $a_2/a_1 \leq 0.4$. This set of criteria has been implemented to treat the coalescence of unequal-sized pits for various a_2/a_1 values. The dimensions of the coalesced pit are taken as: (1) depth = depth of larger pit or microcrack (b_1), and (2) pit width $= 2w = 2a = 2a_1 + 2a_2 + \varepsilon a_1$. The coalescence of pits and microcracks are treated using the same approach on the basis that pit width = pit diameter.

3.2. Stress concentration at pits

The stress concentration factors of hot corrosion pits in ME3 reported in the literature [7,21] were reviewed to gain a perspective on how elastic stress concentration at the pits can affect nucleation and growth of small fatigue cracks at the pits. The results in the literature show that k_t values induced by the hot pits are in the range of 1.36 to 2.85 with an average value of about 2.15 [21]. For a single pit with a pit diameter of $2w$ on the surface and a depth d, the elastic stress concentration factor (k_t) at the pit tip is given by [8]

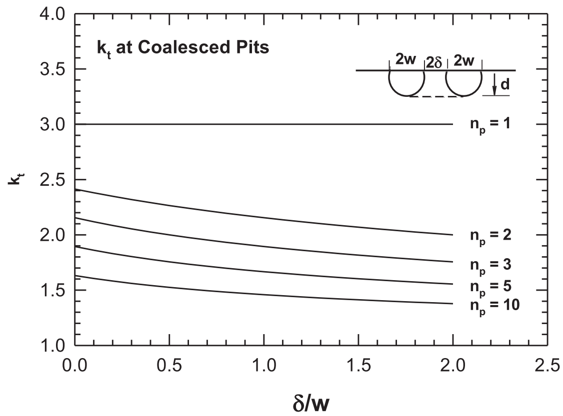

Fig. 5. Stress contraction factor for a coalesced pit as a function of normalized pit spacing for values number of pits involved in the coalescence process.

$$k_t = 1 + 2\sqrt{\frac{d}{w}} \tag{4}$$

which gives a value of 3 for a semispherical pit ($d/w = 1$). For a pair of pits with closely-spaced semispherical pits with depth d, width $2w$, and spacing 2δ, the inner tips located at the ligament of the two pits would interact and join together when the two pits are sufficiently close together. The dimension of the coalesced pit then has a depth of d but a width of $4w + 2\delta$, leading to an elastic stress concentration factor of

$$k_t = 1 + 2\sqrt{\frac{d}{2w + \delta}} \tag{5}$$

which can be generalized to

$$k_t = 1 + 2\sqrt{\frac{d/w}{n_p + \delta/w}} \tag{6}$$

for n_p pits. Eq. (6) indicates that the stress concentration factor of a coalesced pit depends on the pit depth, pit width, number of pits, and the pit spacing. Fig. 5 shows the dependence of k_t on the normalized pit spacing δ/w for n_p values ranging from 1 to 10. Fig. 5 shows that k_t decreases with increasing n_p and δ/w values because the coalesced pit becomes shallower as either n_p or δ/w increases when d is held constant. Instead of a k_t of 3, coalesced pits can exhibit k_t values ranging from 1.5 to 2.4, which are in agreement with those reported by Telesman et al. [21] for coalesced pits with small overlaps. Specifically, Telesman et al [21] analyzed the stress concentrated factors of coalesced pits using FEM analyses. They reported $\mathrm{k_t}$ values of 2 to 2.7 for 2 pits with no overlaps. Furthermore, they reported $\mathrm{k_t}$ values of 1.4 to 1.5 for 6 pits with 1/3 overlaps.

For nucleation of a small fatigue crack from a pit, the threshold stress range is given by [22]

$$\Delta S_{th} = \frac{\Delta\sigma_e}{k_t} \tag{7}$$

where $\Delta\sigma_e$ is the fatigue limit which is estimated to be 700 MPa for ME3. Once nucleated from the pit, the growth of the small crack away from the pit is likely to be controlled by fatigue crack growth threshold, ΔK_{th}, and the notch stress field associated with the pit. According to the worst-case notch analysis [22], the threshold stress for the growth of a small crack away from the pit is given by [22]

$$\Delta S_{th} = \frac{\Delta K_{th}}{F\sqrt{\pi}(\sqrt{d} - \sqrt{a_o})} \tag{8}$$

where F is the boundary-correction factor and a_o is the small-crack parameter. The small-crack parameter is related to the fatigue limit and the large-crack fatigue crack growth (FCG) threshold according to [23]

$$\Delta K_{th} = F\Delta\sigma_e\sqrt{\pi a_o} \tag{9}$$

The condition for the nucleation and growth of a small crack without arrest in a fatigue specimen subject to an remotely applied stress range, $\Delta\sigma$, can be obtained by setting Eq. (7) = Eq. (8) and combining the results with Eq. (9) to give

$$d = (k_t - 1)^2\left[\frac{\Delta\sigma_e}{\Delta\sigma}\right]^2 a_o \tag{10}$$

which can be used to compute d at the onset of fatigue crack nucleation and growth as a function of k_t. Fig. 6 presents k_t as a function of pit depth computed based on Eq. (10) using the appropriate values of $\Delta\sigma_e$ (700 MPa), $\Delta\sigma$ (1131 MPa), and ΔK_{th} (9 MPa(m)$^{1/2}$) for a single semi-circular pit with $d/w = 1$, $F = 0.6758$, and $a_o = 115.21$ μm. As shown in Fig. 6, the theoretical curve follows fairly well

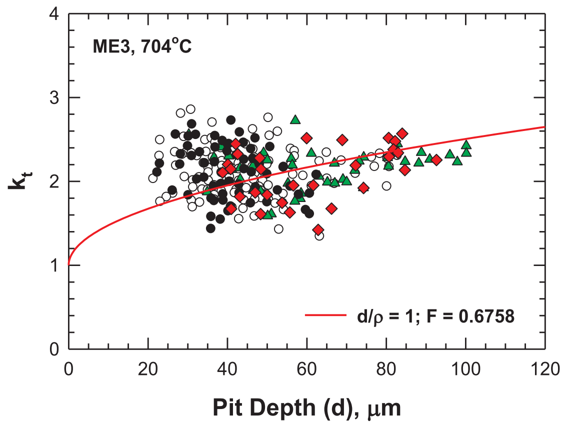

Fig. 6. Observed stress concentration factors as a function of pit depth compared to theoretical curve based on a single semi-circular surface pit computed via Eq. (10). Multiple symbols represent multiples set of pit measurements from Gabb et al. [7].

the general trend of k_t values computed on the basis of Eq. (4) using experimental data of pit depth and pit width from Gabb et al. [7]. The experimental k_t values show substantial variations at low pit depth but the scatter diminishes with increasing pit depth. This finding suggests that there may be more pit interactions at shallow pit depths and pit interactions diminish with increasing pit depths until a few pits become more prominent.

3.3. Fatigue crack nucleation from pits

Crack nucleation from corrosion pits is treated by considering the pits act as stress concentration sites where fatigue cracks nucleate. The mechanism-based crack nucleation model utilized in HOTPITS is given by [24]

$$N_i^S = \left[\frac{\zeta_S}{\left(\frac{2k_t\sigma_a}{F_m} - 2Mk\right)}\right]^{1/\alpha} \tag{11}$$

$$\text{with} \quad \zeta_S = \left[\frac{8M^2\mu^2}{\lambda'\pi(1-\nu)}\right]^{1/2}\left(\frac{h}{D}\right)\left(\frac{c}{D}\right)^{1/2} \tag{12}$$

$$\text{and} \quad F_m = 1 - \left(\frac{\sigma_m}{\sigma_{UTS}}\right)^{\beta} \tag{13}$$

where the material parameters and the corresponding values for slip band crack nucleation at specimen surfaces are defined and summarized in Table 1. The information on the average grain size and the as large as (ALA) grain size were taken from Gabb et al. [25] and Telesman et al. [21]. The model was first fitted to the low-cycle fatigue (LCF) life data [7,21] for uncorroded LCF specimens using a crack length of 1500 µm for LCF failure and a slip band width of 0.1 µm, using a stress concentration factor, k_t, of 1 for smooth

Table 1
Model parameters and their corresponding values for supersolvus materials of ME3 at 704 °C. The k_t value is taken to be 1 for uncorroded LCF specimens and 1.4 for pre-corroded LCF specimens.

ME3	704 °C	Supersolvus	Surface Slipband
Parameter	Symbol	Unit	Value
Shear modulus	μ	MPa	7.07E+04
Poisson's ratio	ν	–	0.33
Fatigue life exponent	α	–	0.3072
Taylor factor	M	–	3.06
Fatigue limit	Mk	MPa	650
Slipband width	h	µm	0.1
Average grain size	D	µm	27.5
As Large As (ALA) grain size	D_{ALA}	µm	90
Half-length at fracture	c	µm	1500
Universal constant	λ	–	0.005
Mean stress to UTS ratio	σ_m/UTS	–	0.29
Mean stress exponent	β	–	1
Stress concentration factor	k_t	–	1 or 1.4

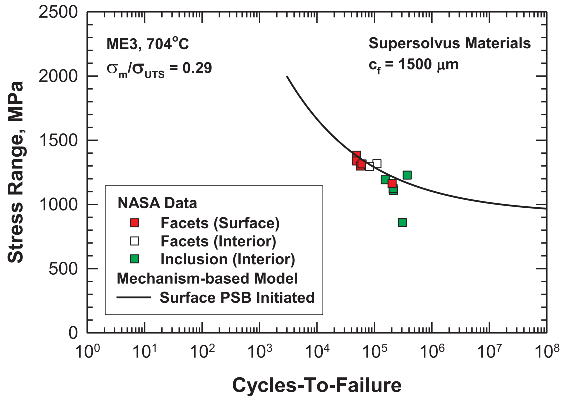

Fig. 7. Comparison of measured and computed stress-life (S-N$_f$) curves for ME3 at 704 °C. The crack nucleation model was fitted to the experimental data of uncorroded ME3 by adjusting the slip band width (h) parameter and crack length (c$_f$) at fracture.

uncorroded specimens. Fig. 7 presents the fit of the model to the LCF model in a stress-life (S-N$_f$) plot, where the stress ranges are those of the first cycle.

The LCF life of corroded ME3 specimens was predicted from Eq. (11) by using an appropriate k_t value. The k_t value for a single semi-ellipsoidal pit can be as high as 3. The k_t values for corroded specimens with complex shapes are lower because of deviations from the semi-spheroidal shape. Telesman et al. [21] have analyzed the k_t values for a series of actual corrosion pits in ME3. They reported k_t values ranging from 1.2 to 1.65, with an average value of 1.4 [21]. The corresponding LCF lives of the corroded ME3 specimens were also reported. To test the validity of Eq. (11) for pre-corroded specimen, a value of $k_t = 1.4$ was utilized to predict the LCF lives of pre-corroded ME3 and the results are compared in Fig. 8 with those reported by Gabb et al. [7] and Telesman et al. [21]. Fig. 8 shows that the agreement between model prediction and experimental data is generally good and consistent with k_t values in the range of 1.2–1.65. The predicted curves for crack nucleation (S-N$_i$) curves in Fig. 8 were computed based on a pit depth (d) of 27.5 μm and a crack depth of 27.5 μm, where 27.5 μm corresponds to the average grain size.

3.4. Pit-to-crack transition

The nucleation of a fatigue crack from a single or coalesced pit can be treated using Eq. (11) and the stress concentration factor is given by Eq. (6). After fatigue crack nucleation from the pit, the crack increment is Δa and the cycle to crack nucleation is N_i^S. The

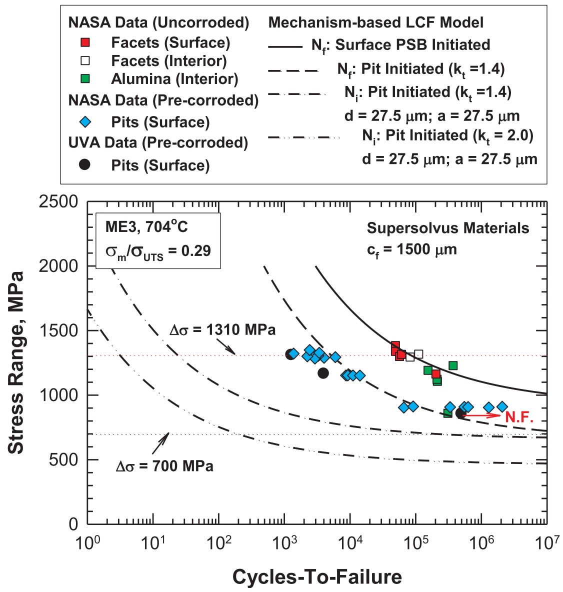

Fig. 8. Comparison of measured and predicted stress-life (S-N$_f$) curves for pre-corroded and uncorroded ME3 fatigue at 704 °C. Mode predicted for the pre-corroded specimens was based on a k_t value of 1.4 and the model constant in Table 1. Experimental data are from [7,21] for the uncorroded condition and from [21] for the pre-corroded conditions. The predicted curves for crack nucleation (S-N$_i$) curves are computed based on a pit depth (d) of 27.5 μm and a crack depth of 27.5 μm, where 27.5 μm corresponds to the average grain size.

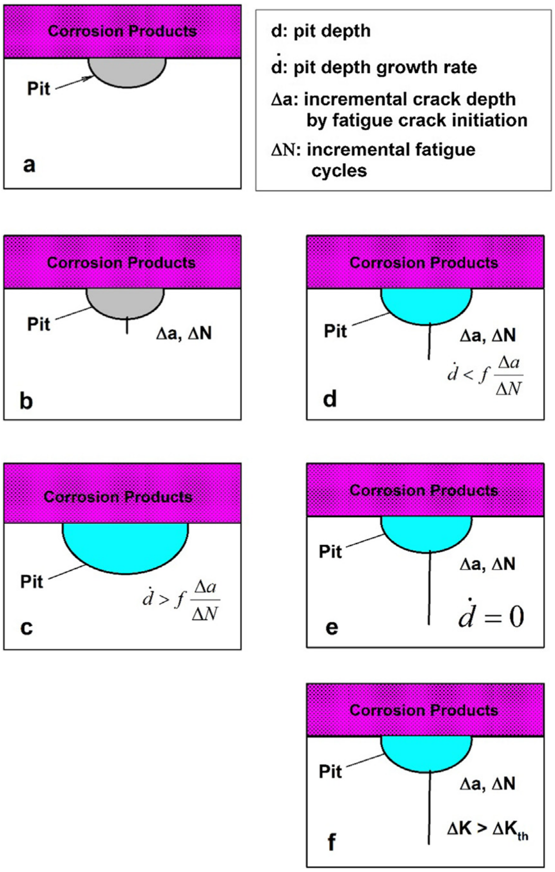

Fig. 9. An updated pit-to-crack transition based on the consideration of pit growth rate ($\dot{d}$) and an apparent "crack nucleation rate" ($\Delta a/\Delta N$) due to fatigue crack nucleation under cyclic frequency f: (a) a hot corrosion pit, (b) the formation of a small crack length, Δa, after ΔN fatigue cycles, (c) removal of Δa by pit growth when $\dot{d} > f\Delta a/\Delta N$ for an active pit, (d) formation of a fatigue crack at the pit bottom of an active pit when $\dot{d} < f\Delta a/\Delta N$ during the same period of hot corrosion, (e) pit-to-crack transition by fatigue crack nucleation for an inactive pit with $\dot{d} \approx 0$, and (f) fatigue crack growth to failure at $\Delta K > \Delta K_{th}$. Thus the pit-to-crack transition needs to be defined in terms of $\dot{d}$, $\Delta a/\Delta N$, ΔK_{th}, the fatigue limit, and the elastic stress concentration factor, k_t, due to the pit.

corresponding crack nucleation rate can be defined as

$$\frac{\Delta a}{\Delta t} = fd_o\left[\frac{\zeta_S}{(k_t\Delta\sigma - \Delta\sigma_e)}\right]^{-1/\alpha} \tag{14}$$

where f is frequency associated with a fatigue cycle and d_o is the initial pit depth after pit formation. The crack nucleation rate can then be utilized to compared against the pit growth rate, $\dot{d}$, using the relation given by

$$\dot{z} = \dot{d} - \frac{\Delta a}{\Delta t} \tag{15}$$

which can be used to discern whether or not the fatigue nucleated crack increment is removed by pit growth. The fatigue crack increment is removed by pit growth when Eq. (15) is negative, and the fatigue crack increment extends beyond the pit when Eq. (15) is positive. Furthermore, the pit growth rate also needs to be compared against the fatigue crack growth rate (da/dt) and the large-crack fatigue threshold to discern whether or not these two conditions are met: (1) the fatigue crack growth rate exceeds the pit growth rate, as given by

$$da/dN > \dot{d} \tag{16}$$

and (2) the stress intensity factor range at the crack tip exceeds the large-crack fatigue crack growth threshold, as given by

$$\Delta K > \Delta K_{th} \tag{17}$$

If both conditions are met, the fatigue crack is allowed to propagate to failure and a hot corrosion fatigue life is computed. The envisioned pit-to-crack transition processes are illustrated schematically in Fig. 9.

For an arbitrary pit subjected to a stress range ΔS, the pit-to-crack transition can be considered to occur at

$$\Delta S \geqslant \Delta S_{th} = \frac{\Delta K_{th}}{F\sqrt{a_o + d + \Delta a}} \tag{18}$$

where Δa is the crack depth of an incipient fatigue crack nucleated at the bottom of a corrosion pit. The corresponding crack nucleation rate ($\Delta a/\Delta t$) at the bottom of the pit is given by

$$\frac{\Delta a}{\Delta t} = \left(\frac{D}{N_i^s}\right)\left(\frac{n_L}{t_{mp}}\right) \tag{19}$$

where D is grain size, N_i^s is the cycles-to-nucleation for a slip band fatigue crack, n_L is the number of load steps, and t_{mp} is the duration of the mission. The cycles-to-nucleation is computed from Eq. (11) to Eq. (14). The pit growth rate ($\Delta d/\Delta t$) in HOTPITS is described in terms of a power-law and it can be expressed as

$$\frac{\Delta d}{\Delta t} = \frac{n_1 d}{t} \tag{20}$$

where n_1 is the time exponent for pit depth growth and t is the time of hot corrosion. During active hot corrosion involving concurrent fatigue crack nucleation from active pits, the transition from pit-to-crack is envisioned to occur when the fatigue crack nucleation rate exceeds the pit growth rate. On this basis, the critical condition for the pit-to-crack transition can be determined from Eq. (18) and Eq. (19) according to the inequality given by

$$\frac{\Delta a}{\Delta t} \geqslant \frac{\Delta d}{\Delta t} \tag{21}$$

which may be combined with Eqs. (21) and (22) to arrive at the critical condition for the pit-to-crack transition, which is given by

$$d \geqslant d_{crit} \tag{22}$$

$$\text{with} \quad d_{crit} = \left(\frac{D}{N_i^s}\right)\left(\frac{n_L}{t_{mp}}\right)\left(\frac{t}{n_1}\right) \tag{23}$$

Eq. (23) indicates that a critical pit depth, d_{crit}, occurs beyond which a pit would nucleate a fatigue crack at the bottom of a growing pit and the fatigue crack is capable of outrunning the advancing pit. At $d \leq d_{crit}$, a fatigue crack nucleating from the bottom of a pit would be removed by the advancing pit because the pit grows at a higher rate than a fatigue crack can be nucleated. At $d > d_{crit}$, a pit nucleates a fatigue crack of incremental length Δa at a faster rate than the pit can advance. As a result, a fatigue crack of length ($\Delta a - \Delta d$) forms ahead of the pit. Fig. 10 depicts the pit-to-crack transition established on the basis of Eqs. (22) and (23). Fig. 10 shows that d_{crit} is defined by the condition when $\Delta d/dt = \Delta a/\Delta t$. At $d \leq d_{crit}$, pit growth dominates when $\Delta d/\Delta t > \Delta a/\Delta t$. In contrast, fatigue crack nucleation dominates when $d > d_{crit}$ by virtue of $\Delta a/\Delta t > \Delta d/\Delta t$.

Fatigue cracks nucleating at the bottom of a pit may not grow since the applied stress range might lie below the threshold stress range for the growth of a large crack. To meet the threshold stress criterion for large-crack growth, the pit depth (d) or the nucleated crack depth (Δa) in Eq. (18) must increase with time. This may require continual fatigue crack nucleation at the pit bottom or through a process of pit or crack coalescence. Eventually, Eq. (18) is met and the fatigue crack growth threshold boundary is exceeded and the nucleated fatigue crack propagates as a large crack. The transition from a pit to a large crack is determined from Eq. (18). This process of pit-crack transition involving fatigue crack nucleation and coalescence, as well as the transition to a large crack, has been implemented into the HOTPITS prototype.

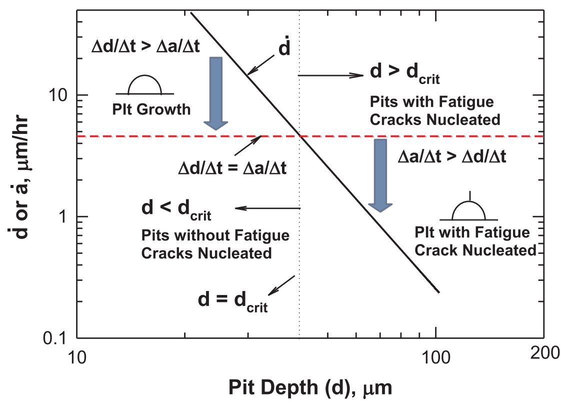

Fig. 10. Plot of $\Delta a/\Delta t$ or $\Delta d/\Delta t$ versus pit depth (d) illustrating the dependence of pit-to-crack transition on the critical pit depth, d_{crit}.

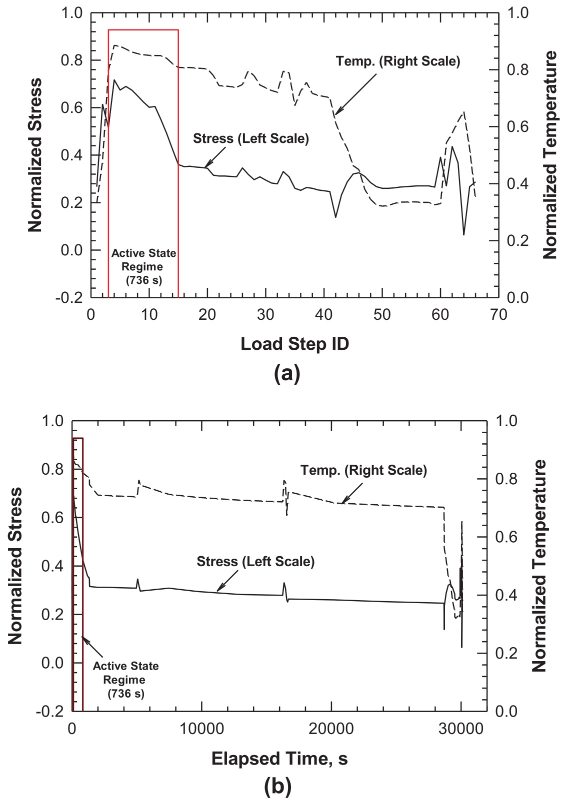

Fig. 11. Mission profiles showing temperatures and stresses as a function of load steps in (a) and elapsed times in (b). The active state region where hot corrosion is operative is highlighted.

3.5. Modeling of corrosion fatigue crack growth

The current DARWIN platform allows users to treat multiple damage modes including cycle-dependent crack growth and time-dependent crack growth. In general, the crack growth increment (da) during an arbitrary fatigue cycle and duration can be expressed as [15,26]

$$da = \left(\frac{da}{dN}\right)dN + \left(\frac{da}{dt}\right)dt \tag{24}$$

where da/dN and da/dt represent cycle-dependent and time-dependent crack growth rates, respectively. Cycle-dependent crack growth is typically described in terms of the Paris power-law equation as given by

$$\left(\frac{da}{dN}\right) = A\Delta K^n \tag{25}$$

$$\left(\frac{da}{dN}\right) = 0 \ \text{ for } \ \Delta K < \Delta K_{th} \tag{26}$$

where A and n are empirical constants. Appropriate material constants in the Paris Power-Law equation were obtained for ME3 as a function of temperature. Fit of Eq. (27) to experimental da/dN data at a stress ratio, R, of 0.5 for ME3 was reported earlier by Chan et al. [15,26]. Time-dependent crack growth is also described in terms of a power-law equation as given by [15,26]

$$\left(\frac{da}{dt}\right) = BK^m \tag{27}$$

$$B = B_o \exp(-Q/RT) \tag{28}$$

$$\left(\frac{da}{dt}\right) = 0 \ \text{ for } \ K < K_{th} \tag{29}$$

where B_o and m are empirical constants; Q is the activation energy. Appropriate material constants in the time dependent power-law equation were obtained for ME3 and they are as follow: $B_o = 1.116E + 5$ mm/s, $Q = 316.36$ KJ/mol K, $m = 5.388$, and

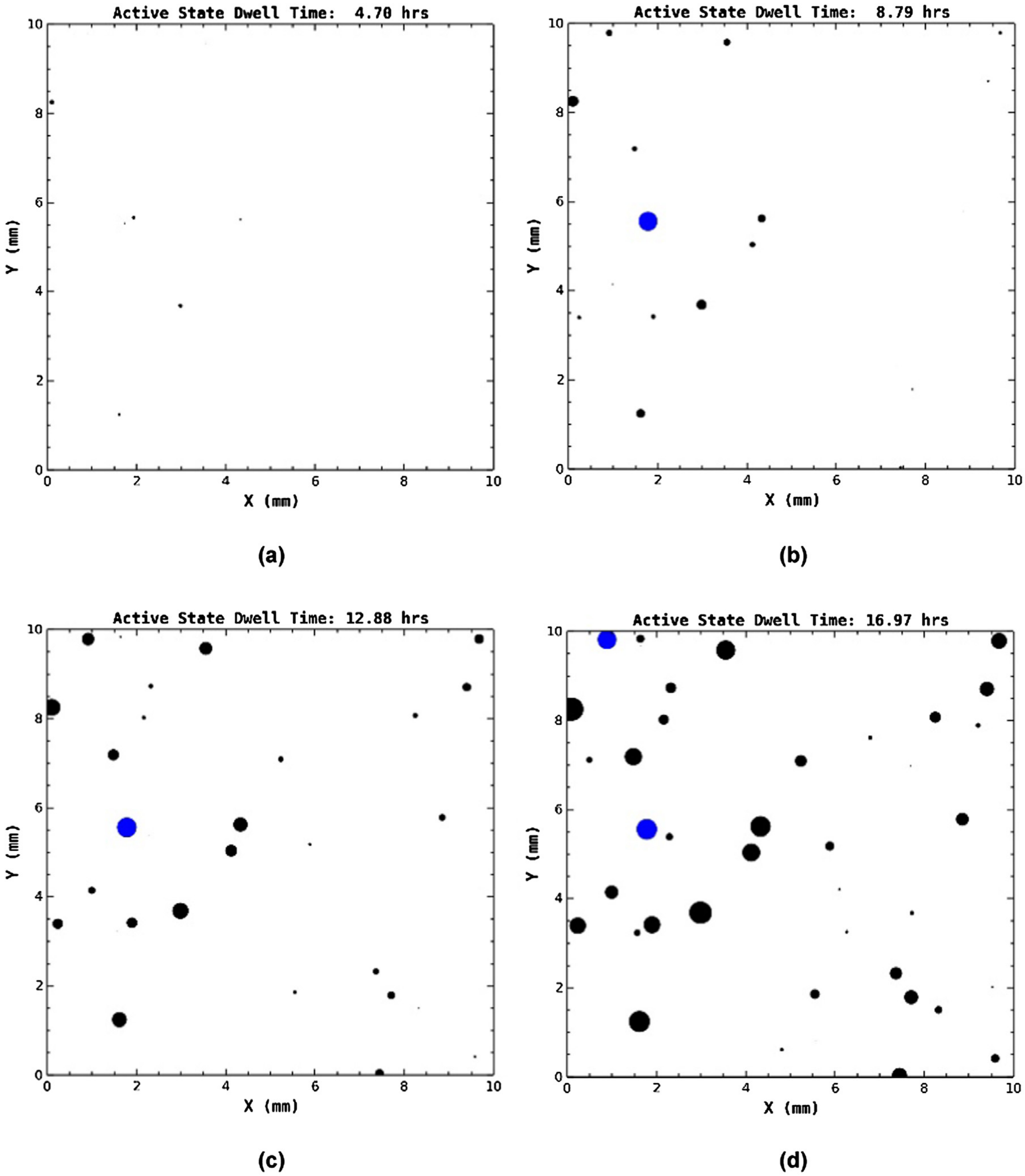

Fig. 12. Hot corrosion processes simulated in the benchmark demonstration problem: (a) pit nucleation at an accumulated dwell time of 4.7 h, (b) pit growth at an accumulated dwell time of 8.79 h, (c) pit nucleation, growth, and coalescence at a dwell time of 12.88 h, and (d) at a dwell time of 16.97 h.

K_{th} = 19.2 MPa√m [15,26]. Applications of Eq. (24) to Eq. (29) to hot corrosion fatigue crack growth can be found in the paper by Chan et al. [15,26].

4. Benchmark hot corrosion simulation

A benchmark problem involving a realistic mission profile was selected and utilized to verify that the HOTPITS prototype software functioned as it was intended. The temperature and stress profiles selected for this benchmark calculation are presented in Fig. 11(a) and (b) in terms of the load step number and elapsed time, respectively. Both the temperatures and stresses have been normalized for

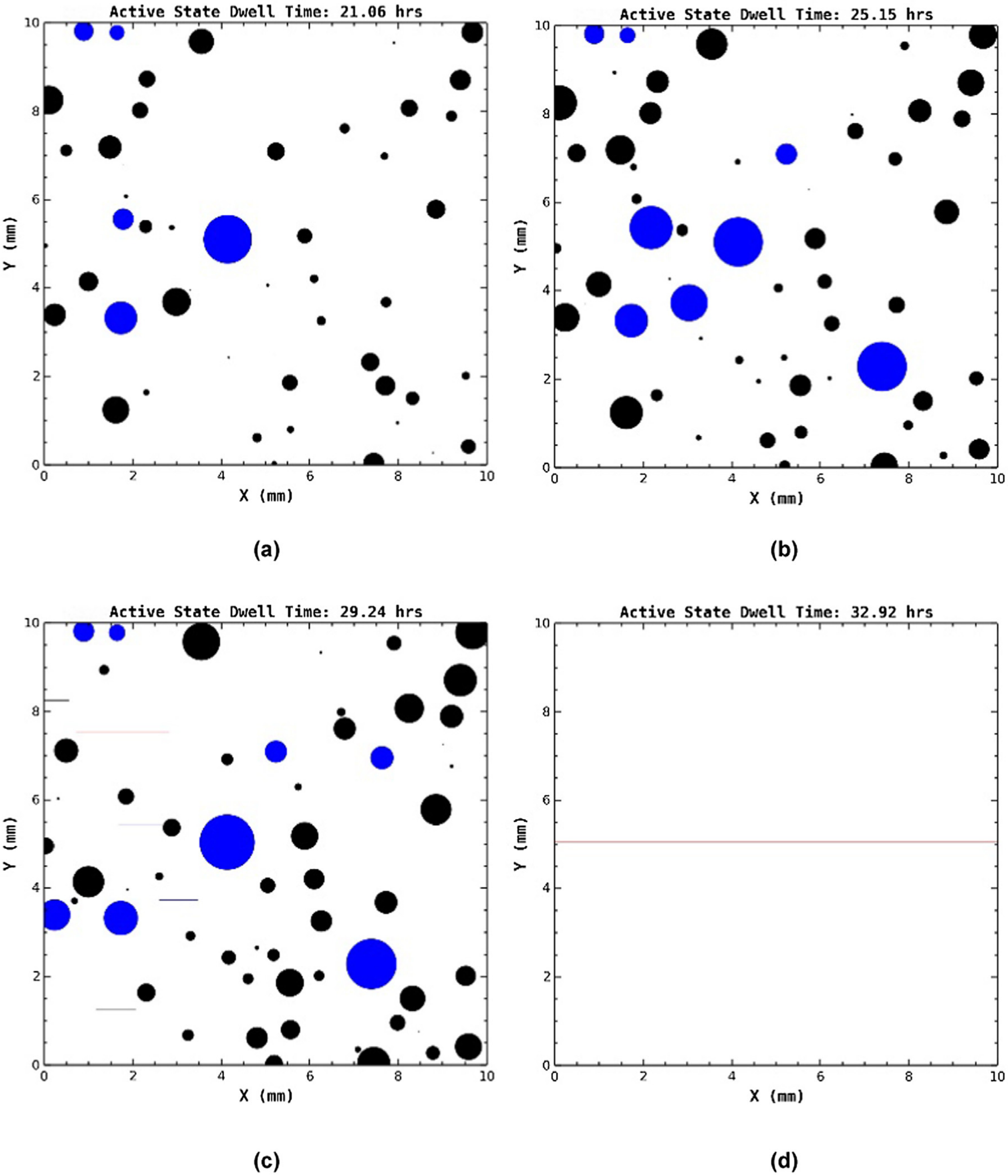

Fig. 13. Hot corrosion processes simulated in the benchmark demonstration problem: (a) pit nucleation, growth, and coalescence at a dwell time of 21.06 h, and (b) at a dwell time of 25.15 h, (c) pit transition to microcracks at a dwell time of 29.24 h, and (d) the transition to a single propagating fatigue crack.

the fictitious mission profile. Both the temperature and the stress profiles are proprietary information of an industrial partner and can be disclosed only in the normalized forms. One mission (or cycle) corresponds to a complete set of thermal and mechanical load steps presented in Fig. 11(a). The parts of the mission profile where the temperatures are sufficiently high for hot corrosion to take place (active state) are highlighted in Fig. 11(a) and (b) and the active states last about 736 s per mission. The mission profile, referred to as case 1, was applied to a rectangular element 10 mm in width and 10 mm in height [16] and the mission history was repeated until a single crack propagated through the entire element. It is important to note that the hot corrosion mechanisms (pit nucleation, growth, and coalescence) cease to be operative when the temperature is outside the active state region, but they become operative again when

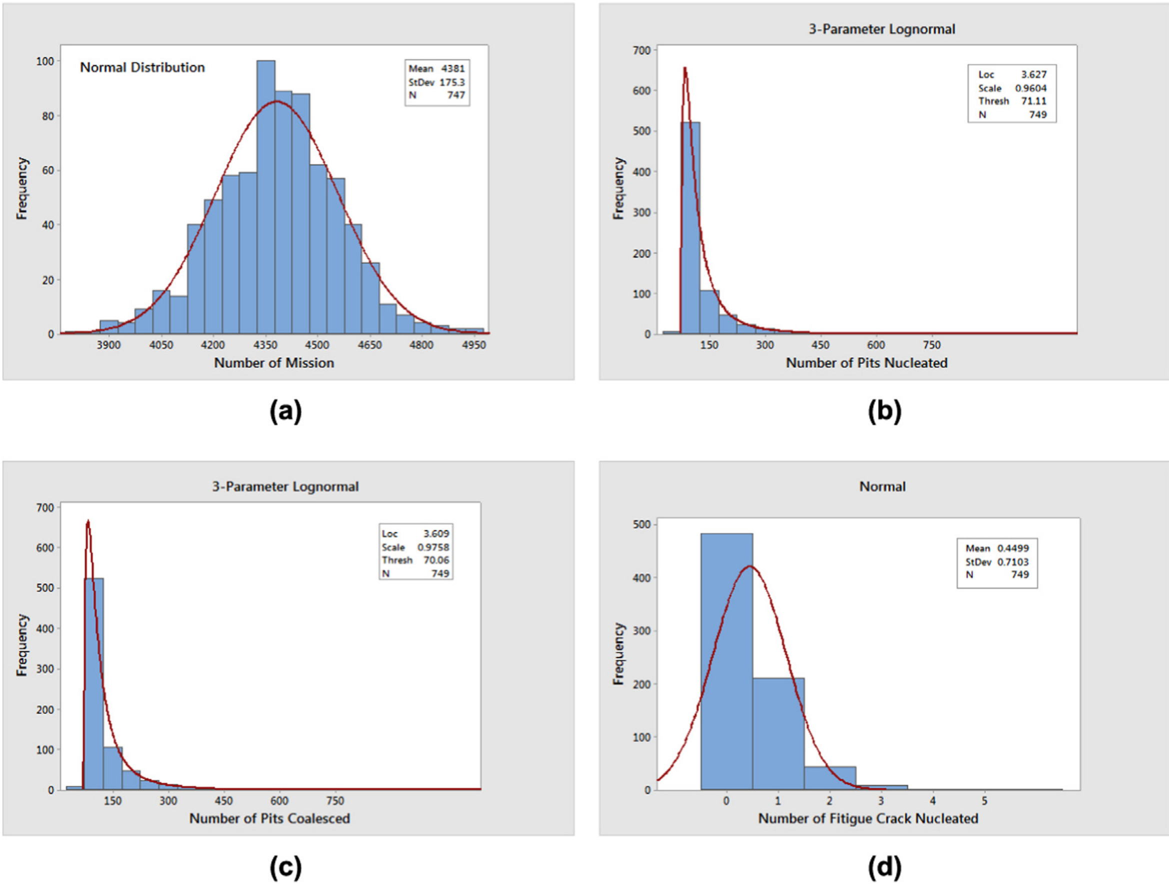

Fig. 14. HOTPITS simulation results for Case 1 with 11 temperature steps in the hot corrosion regime: (a) fatigue life, (b) frequency of number of pits nucleated, (c) frequency of number of pits coalesced, and (d) frequency of number of fatigue cracks nucleated at pits.

the temperature is within the active state in subsequent missions. Outside the active state, fatigue cracks are allowed to nucleate and grow at the bottom of the non-active corrosion pits. The intent of this article is to document the development of the HOTPITS approach. As a result, a realistic mission profile has been used to illustrate the types of temperature and load profiles that can be utilized by HOTPITS. On the other hand, the model constants utilized in the benchmark computations have been chosen to illustrate the various capabilities of the methodology; neither the model constants nor the simulated response correspond to any particular engine components.

Selected results of the benchmark demonstration problem involving pertinent hot corrosion mechanisms during the fictitious mission are presented in Fig. 12 for various accumulated dwell times within the active state region. Fig. 12(a) shows the nucleation of individual hot corrosion pits at a dwell time of 4.7 h. The subsequent growth of these individual pits, the continuous nucleation of additional pits, and the coalescence of closely spaced pits at a dwell time of 8.79 h are presented in Fig. 12(b). In Fig. 12(b), the blue dots (on-line version) represent coalesced pits while the black dots represent individual pits with growth but without coalescence. Subsequent pit nucleation, growth, and coalescence are presented in Fig. 12(c) and (d) for accumulated dwell times of 12.88 h and 16.97 h, respectively.

Hot corrosion continued by pit nucleation, growth, and coalescence without forming a fatigue crack, as illustrated in Fig. 13(a) and (b) for accumulated dwell times of 21.06 h and 25.15 h, which are the equivalent of 105 and 125.75 flight cycles, respectively. Transition of pits to fatigue cracks is observed at an accumulated dwell time of 29.24 h, as shown in Fig. 13(c), and a single fatigue crack is formed at a dwell time of 32.92 h, Fig. 13(d).

To assess the role of temperature on hot corrosion fatigue life, a second benchmark problem involving a realistic mission profile was performed to verify that the HOTPITS prototype software functioned as it was intended for both active and non-active hot corrosion states. This was accomplished by modifying the temperature profile shown in Fig. 11 (Case 1) such that only one load step (Case 2) was operative in the hot corrosion regime [13]. In particular, the number of load steps in the active states was 11 in Case 1 while it was 1 in Case 2. The same stress histories were used for base Case 1 and Case 2. The random variables in these simulations were the sulfate layer thickness and the location where pitting occurred. The intent of the Case 2 simulation was to increase the number of fatigue cracks nucleated at the bottom of the corrosion pits and to verify the pit-to-crack transition for non-active states where fatigue crack nucleation and growth may dominate the hot corrosion process.

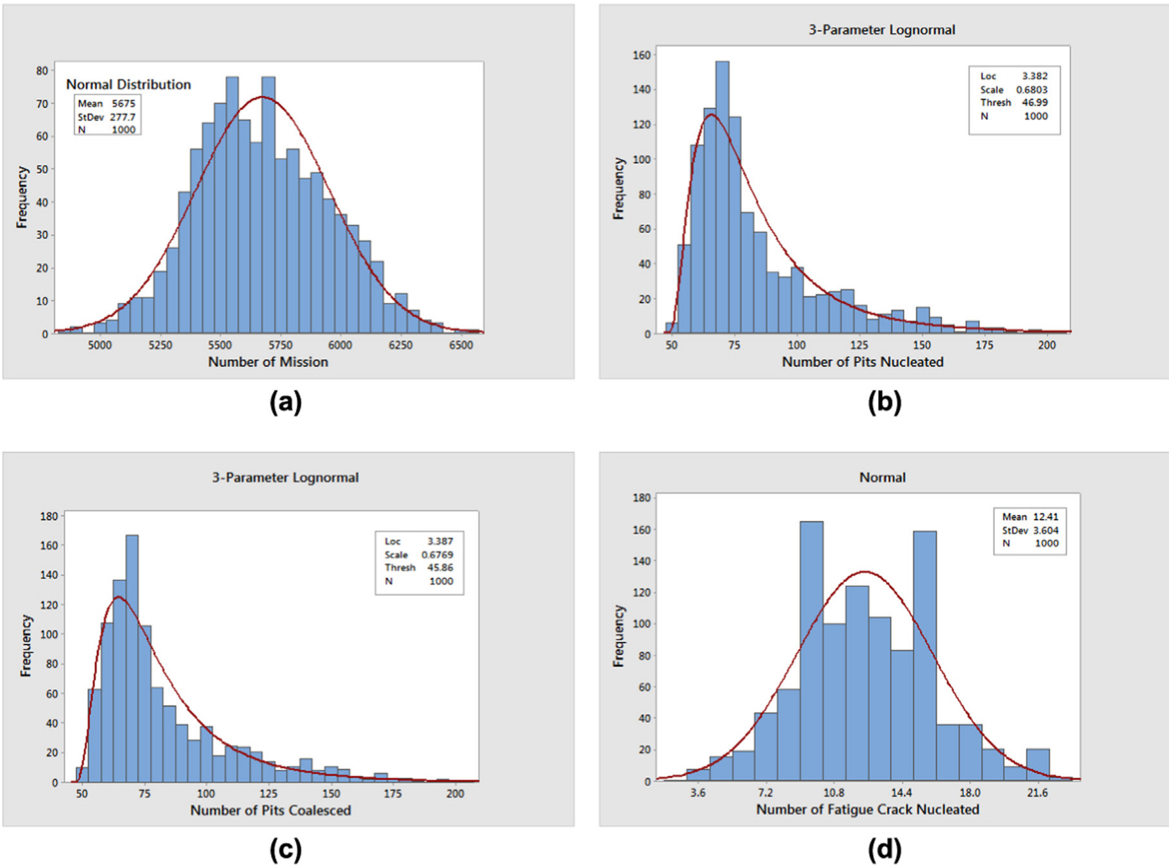

Fig. 15. HOTPITS simulation results for Case 2 with 1 temperature step in the hot corrosion regime: (a) fatigue life, (b) frequency of number of pits nucleated, (c) frequency of number of pits coalesced, and (d) frequency of number of fatigue cracks nucleated at pits.

Fig. 14(a), (b), (c), and (d) present the cycles to failure (number of mission), number of pits nucleated, number of pits coalesced, and number of fatigue crack nucleated at pit(s) in a mission, respectively, for Case 1 where there were 11 temperature steps in the active hot corrosion regime. The total number of missions was 749. No failure was observed in two missions and these two cases were not considered in the fatigue life distribution. Fig. 14(a) shows that the mean fatigue life was 4381 with a life distribution adequately described as a normal distribution. Both the number of pits nucleated or coalesced can be described in terms of 3-parameter lognormal distributions, as shown in Fig. 14(b) and (c). Fig. 14(d) presents the frequency of missions as a function of number of fatigue cracks nucleated at pits. For a majority of missions, the number of fatigue cracks nucleated is zero and the pits transition directly to a large crack without fatigue crack nucleation. In addition, the frequency decreases rapidly with increasing number of fatigue cracks nucleated. The number of missions with four or more fatigue crack nucleation events is essentially zero.

In comparison, Fig. 15(a), (b), (c), and (d) present the cycles to failure (number of mission), number of pits nucleated, number of pits coalesced, and number of fatigue crack nucleated at pit(s) in a mission, respectively, for Case 2 where there was 1 temperature step in the active hot corrosion regime. The total number of missions was 1000 and all 1000 missions showed fatigue failure. Fig. 15(a) shows that the mean fatigue life is 5675 and the lives are well described by a normal distribution. Both the number of pits nucleated or coalesced can be described in terms of 3-parameter lognormal distributions, as shown in Fig. 15(b) and (c). Fig. 15(d) presents the frequency of missions as a function of number of fatigue cracks nucleated at pits. For Case 2, the mean number of missions with fatigue crack nucleated is 12.4 and the pits transition directly to a large crack through a process of fatigue crack nucleation and coalescence in order to form a large crack. The frequency distribution of the missions with fatigue crack nucleation is also well described by a normal distribution. The simulation results indicate that more missions exhibit fatigue crack nucleation and coalescence when the number of temperature steps in the active hot corrosion regime is reduced from 11 to one. With reduced times spent in the active hot corrosion regime, more fatigue cracks can be nucleated from the inactive corrosion pits.

Fig. 16(a), (b), and (c) present the results of defect areas as a function of number of flight cycle. Fig. 16(a) shows the defect areas during pit growth for Case 1 and Case 2. There is more pit growth in Case 1 because more temperature steps are spent in active states. Fig. 16(b) shows the transition from the pit growth regime to fatigue crack growth regime. The pit growth regime for Case 1 is smaller compared to that for Case 2 in a plot of defect area vs. fatigue cycles because of a faster pit growth rate and higher pit depth that leads to an earlier transition from a pit to a large crack. Fig. 16(c) present a comparison of the complete defect area vs fatigue cycle curves for Case 1 and Case 2. For both cases, the times spent in pit growth are small compared to the times spent in propagating a large crack

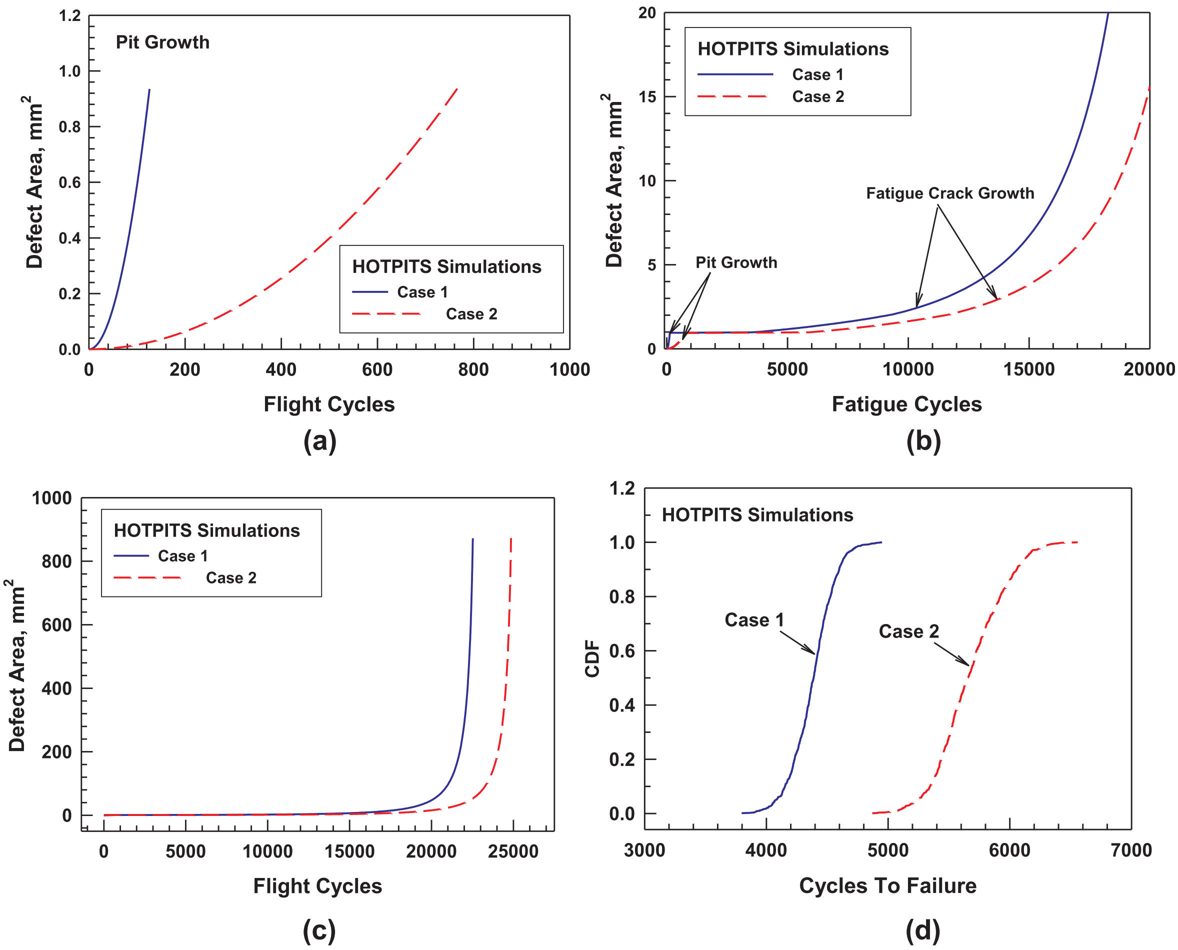

Fig. 16. A comparison of defect areas versus fatigue cycles for Case 1 and Case 2: (a) pit growth regime, (b) pit growth and fatigue crack growth regimes, (c) total lives for Case 1 and Case 2, and (d) a comparison of the CDF curves for Case 1 and Case 2.

to failure. Nonetheless, Case 1 exhibits a shorter fatigue crack growth life compared to that of Case 2, where more load steps are spent in the fatigue regime. The shorter fatigue life in Case 1 can be attributed to a larger pit depth for Case 1, as shown in Fig. 16(a). Fig. 16(d) compares the CDF for Case 1 and Case 2, which shows that the risk to fatigue failure is higher for Case 1 compared to Case 2 due to the presence of more active hot corrosion states, which produce higher pit depths and more pit coalescence.

5. Discussion

Extensive efforts were spent in verifying and validating the various hot corrosion mechanisms observed in the HOTPITS simulations. Fig. 17(a) and (b) show pit nucleation and growth in ME3 at dwell times of 10 and 47 h at the peak stress, respectively. The location where a pit is nucleated has been treated as a random process. Once nucleated, a pit is allowed to grow with time until it impinges on and coalesces with a closely spaced neighboring pit or pits. The coalescence of two closely spaced pits into one large pit is presented in Fig. 17(c) and (d).

The transition of a pit to become a small fatigue crack based on a set of transition criteria based on the large-crack fatigue crack growth threshold and crack growth rate is illustrated in Fig. 18(a) and (b). The coalescence of a corrosion pit with a small fatigue crack is presented in Fig. 18(c) and (d). Closely spaced small fatigue cracks are allowed to interact and coalesce into a larger microcrack, as illustrated in Fig. 19(a) and (b). The microcrack continues to propagate and interact with any cracks or pits along its path, Fig. 19(c), and eventually propagates as a single crack to final fracture, as shown in Fig. 19(d).

The pitting and fatigue mechanisms simulated by HOTPITS are consistent with the hot corrosion mechanisms in ME3 reported by Gabb et al. [7] and Telesman et al. [21], who demonstrated the important role of the stress concentration factor of the evolving pits, which undergo significant changes in morphology due to individual growth and coalescence with other pits. Nucleation of fatigue cracks at coalesced surface pits was also observed in this investigation, as reported by Goodrum et al [13]. For illustration, Fig. 20 shows fatigue nucleation at irregularly-shaped surface pits formed by the joining of two closely spaced smaller semi-ellipsoidal pits. Multiple fatigue cracks are seen to nucleate and propagate from the coalesced pits. These microcracks subsequently linked together to

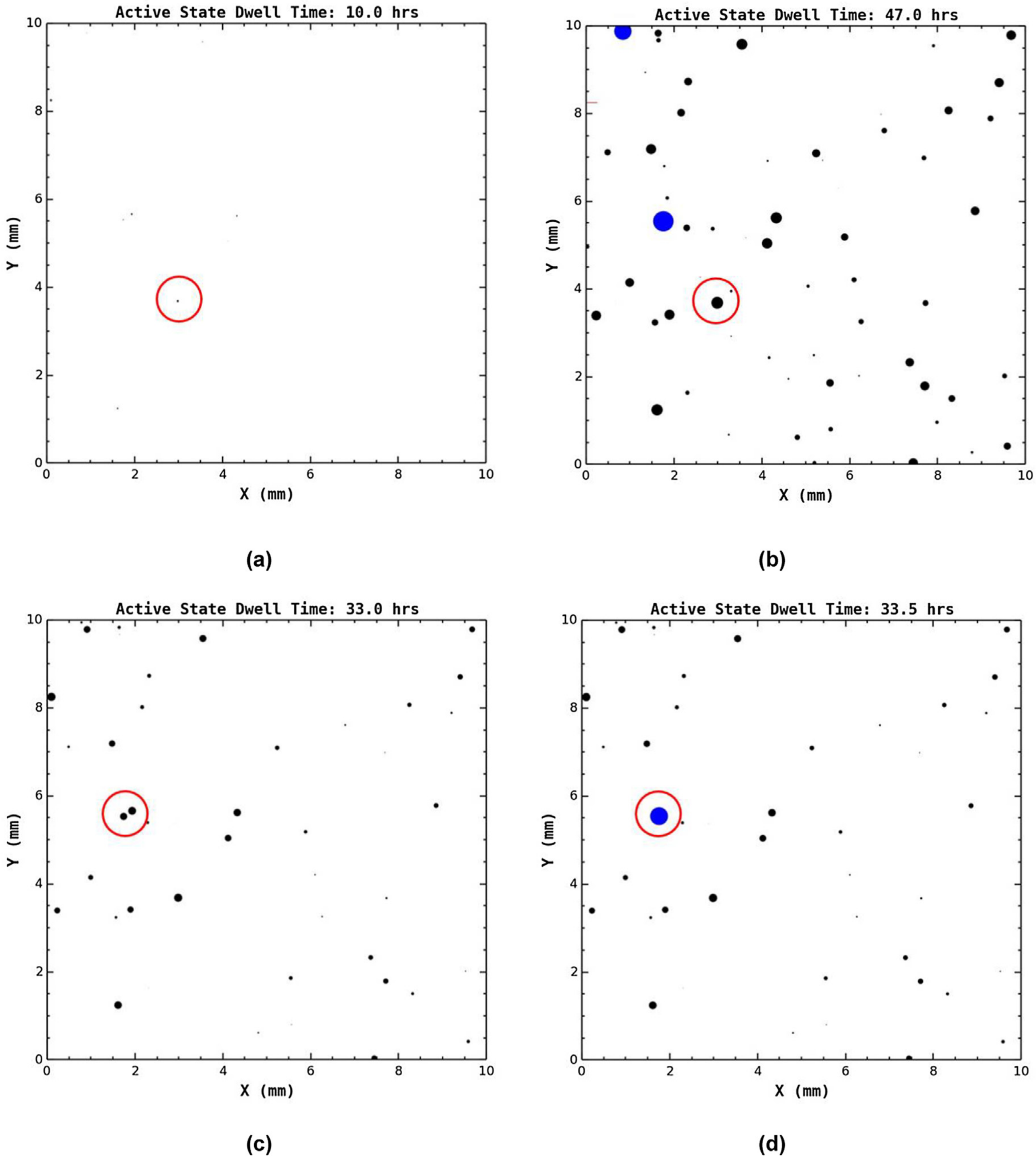

Fig. 17. Hot corrosion mechanisms in HOTPITS prototype: (a) pit nucleation, (b) pit growth, (c) pit interaction, and (d) pit coalescence.

form a large fatigue crack that propagated to fracture. The observed pitting and fatigue processes validated the hot corrosion damage processes implemented in HOTPITS.

6. Conclusions

A probabilistic life-prediction methodology, dubbed HOTPITS, has been extended for treating the evolution of multiple pits during Type II hot corrosion of Ni-based superalloys used in gas turbine engine components. The methodology is capable of predicting the nucleation, growth, and coalescence of multiple pits as a function of service temperature, sulfur contents in fuel, and salt content in air, as well as the transition of pits to microcracks, and the coalescence of microcracks to form a single critical crack that propagates to failure. The HOTPITS methodology has been implemented into a commercial probabilistic life-prediction code called DARWIN. The utility of HOTPITS for predicting the hot corrosion fatigue life of a fictitious gas turbine disk has been demonstrated

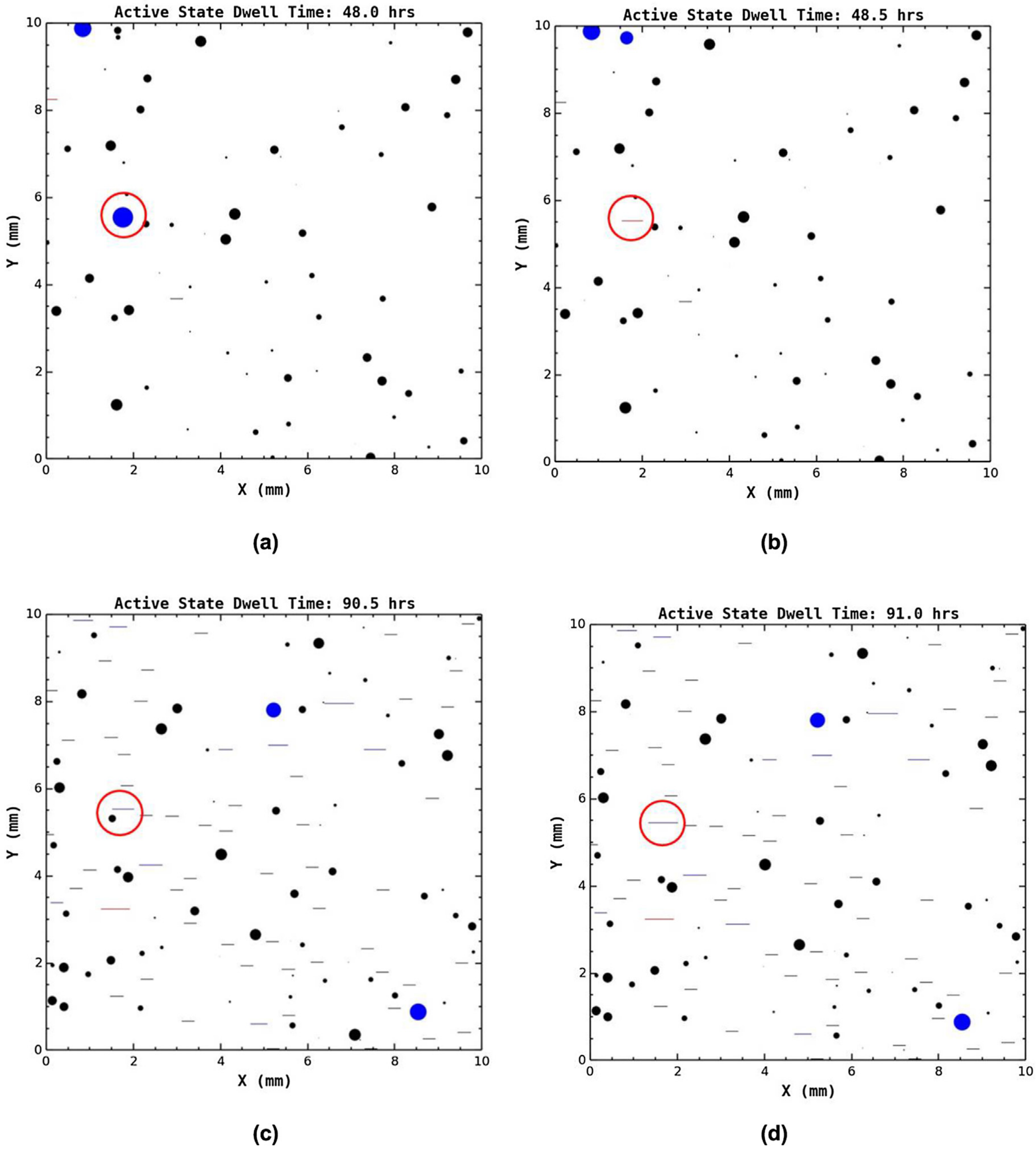

Fig. 18. Transition of a hot corrosion pit to become a fatigue crack: (a) a hot corrosion pit prior to becoming a fatigue crack, and (b) a fatigue crack is formed after the hot corrosion it exceeds the large-crack threshold and the fatigue propagates at a faster rate than the hot corrosion growth rate, (c) interaction between a pit and a microcrack, and (d) linkage of a pit with the microcrack to become a longer microcrack.

using the DARWIN platform. Two benchmark computations were performed to verify the software tools were implemented correctly into DARWIN: (1) one involved load and temperature histories where hot corrosion are always active, and (2) one involved load and temperature histories where hot corrosion pit nucleation, growth, and coalescence are not always active but contain dormant periods.

Declaration of Competing Interest

The authors declare that they have no known competing financial interests or personal relationships that could have appeared to influence the work reported in this paper.

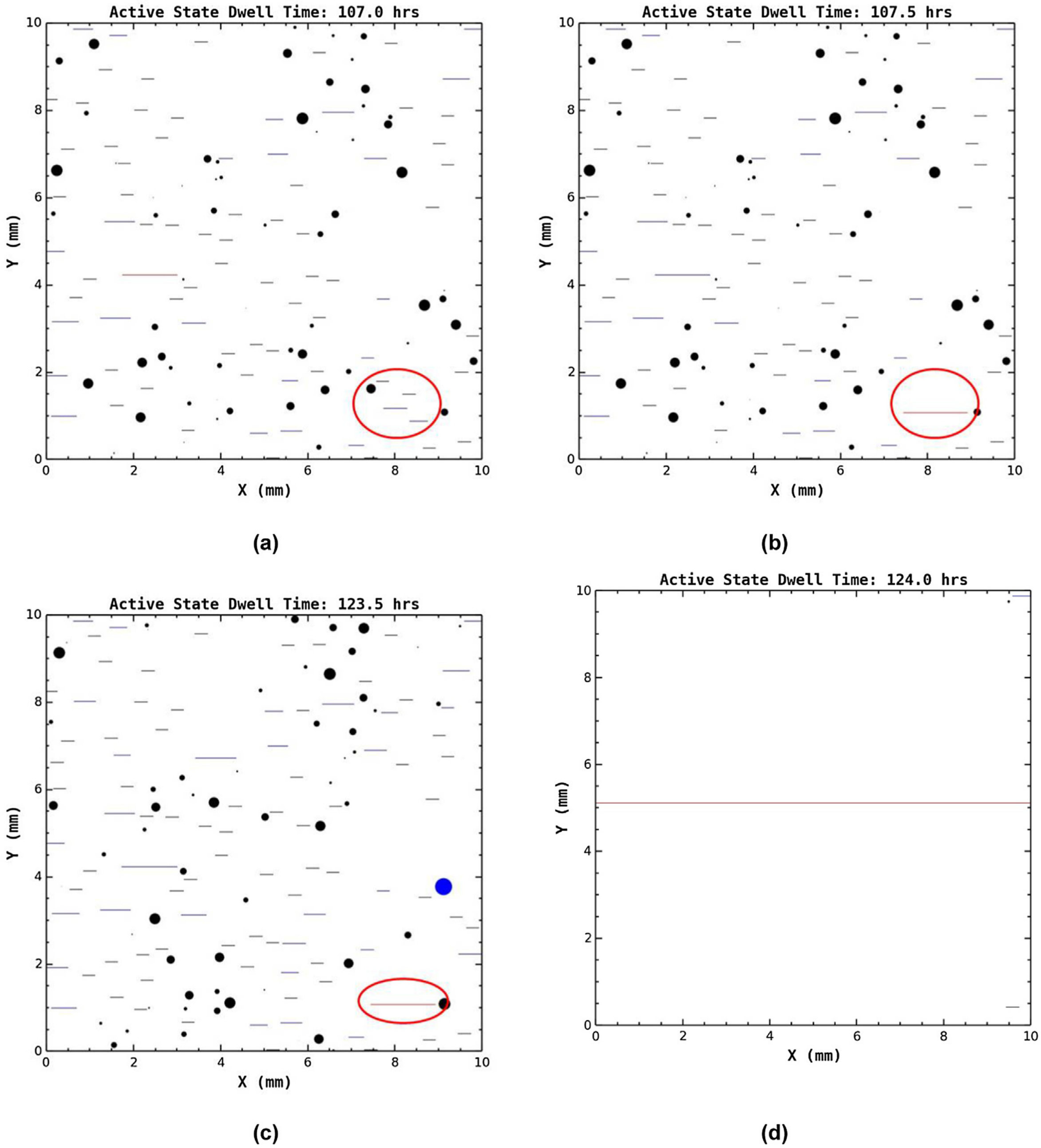

Fig. 19. The linkage of multiple pits and microcrack to form a critical large crack: (a) interaction between pits and microcracks, (b) the pits and the microcracks coalesce to become a longer microcrack, (c) propagation of the longer microcracks to become a critical crack, and (d) propagation of a single critical crack to failure.

Acknowledgements

The authors would like to acknowledge the financial support of the National Aeronautics and Space Administration (NASA) Small Business Technology Transfer (STTR) Program through Contract No. NNX15CC33C and the encouragement by Dr. Jack Telesman, Program Monitor. The funding organization (NASA) had no involvement in the design, collection, analysis, interpretation of data, and development of software tools, or writing of the article. The views, opinions and/or findings expressed are those of the authors and shall not be interpreted as representing the official views or policies of NASA or the US Government. The authors are thankful to Drs. Tim Gabb and Jack Telesman for providing the corrosion fatigue and fatigue life data of ME3 utilized in the model development. The clerical assistance of Ms. Loretta Mesa of Southwest Research Institute (SwRI®) in the preparation of the manuscript is also acknowledged.

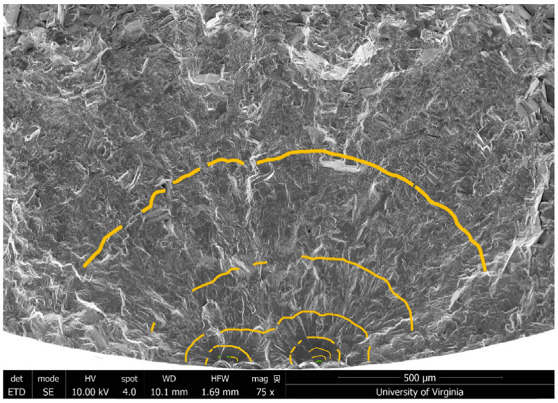

Fig. 20. SEM fractograph illustrates the formation and propagation of fatigue cracks from coalesced pits on a pre-corroded ME3 specimen fatigue tested at 704 °C. The micrograph depicts the nucleation of multiple fatigue cracks from coalesced hot-corrosion pits. The multiple fatigue cracks subsequently coalesced to from a propagating large fatigue crack.

Appendix A. Supplementary material

Supplementary data to this article can be found online at https://doi.org/10.1016/j.engfracmech.2020.106889.

References

[1] Goebel JA, Pettit FS, Goward GW. Mechanisms for the hot corrosion of nickel-based alloys. Metall Trans 1973;4:261–78.
[2] Chiang KT, Pettit FS, Meier GH. Low temperature hot corrosion. In: Rapp RA, editor. High temperature corrosion. NACE-6; 1983. p. 519–30.
[3] Pettit FS, Meier GH. Oxidation and hot corrosion of superalloys. In: Gell M, Kortovich CS, Bricknell RH, Kent WB, Radavich JF, editors. Superalloys 84. Warrendale, PA: TMS; 1984. p. 651–87.
[4] Rapp R. Hot corrosion of materials; a fluxing mechanism? Corros Sci 2002;44:209–21.
[5] Groh JR, Duvelius RW. Influence of corrosion pitting on Alloy 718 fatigue capability. In: Loria LA, editor. Superalloys 718, 625, 706 and various derivatives. Warrendale, PA: TMS; 2001. p. 583–92.
[6] Gabb TP, Telesman J, Kantzos PT, Smith JW, Browning PF. Effects of high temperature exposures on fatigue life of disk superalloys. In: Green KA, Pollock TM, Harada H, Howson TE, Reed RC, Schirra JJ, Watson S, editors. Superalloys 2004. Warrendale, PA: TMS; 2004. p. 269–74.
[7] Gabb TP, Telesman J, Hazel B, Mourer DP. The effects of hot corrosion pits on the fatigue resistance of a disk superalloy. J Mater Engng Perform 2010;19(1):77–89. https://doi.org/10.1007/s11665-009-9399-5.
[8] Birbilis N, Buchheit RG. Measurement and discussion of low-temperature hot corrosion damage accumulation upon nickel-based superalloy René 104. Metall Mater Trans A 2008;39A:3224–32.
[9] Luthra KL, Shores DA. Mechanism of Na_2SO_4 induced corrosion at 600°-900°C. J Electrochem Soc 1980;127(10):2202–10.
[10] Gokoglu SA, Santorp GJ. Experimental verification of corrosive vapor deposition rate theory in high velocity burner rigs. In: Betz W, editor. High temperature alloys for gas turbines and other applications. Dordrecht, Germany: Reidel Publishing Co.; 1987. p. 1117–26.
[11] Leyens C, Wright IG, Pint BA. Hot corrosion of nickel-based alloys in biomass-derived fuel simulated atmosphere. In: Hampikian JM, Dahotre NB, editors. Elevated temperature coatings: science and technology III. Warrendale: TMS; 1999. p. 79–90.
[12] Encinas-Oropesa A, Drew GL, Hardy MC, Leggett AJ, Nicholls JR, Simms NJ. Effects of oxidation and hot corrosion in a nickel disc alloy. In: Reed RC, Green KA, Caron P, Gabb TP, Fahrmann MG, Huron ES, Woodard SA, editors. Superalloy 2008. Warrendale, PA: TMS; 2008. p. 609–18.
[13] Goodrum W, Chan KS, Enright MP, Burns JT, Mills DM. Development of physics-based modeling tools for life-prediction and durability assessment of advance materials. Phase II Final Report. NNX15CC33C, ERI, Charlottesville, VA; 2018.
[14] Southwest Research Institute. "DARWIN® User's Guide", San Antonio, TX; 2013.
[15] Chan KS, Enright MP, Moody JP. Development of a probabilistic methodology for predicting hot corrosion fatigue crack growth life of gas turbine engine disks. J Eng Gas Turbines Power 2014;136(022505):1–8.
[16] Chan KS, Enright MP, Moody JP, Fitch SHK. Physics-based modeling tools for predicting type II hot corrosion in Ni-based superalloys. In: Hardy M, Huron E, Glatzel U, Griffin B, Lewis B, Rae C, Seetharaman V, Tin S, editors. Superalloy 2016. New Jersey: Wiley; 2016. p. 917–25.
[17] Chan KS, Burns JT, Enright MP, Moody JP, Goodrum W. Validation of hot corrosion and fatigue models in HOTPITS. J Eng Mater Tech 2019. https://doi.org/10.1115/1.4045910. Published on-line.
[18] Birks N, Meier GH, Pettit FS. Introduction to the high-temperature oxidation of metals. 2nd ed. Cambridge, UK: Cambridge University Press; 2006. p. 234.
[19] Bol'shakov KA, Fedorov PI. The ternary system of sodium, cobalt and nickel sulfates. J Inorgan Chem USSR 1958;III(8):1896–900.
[20] Murakami Y. Stress intensity factors handbook 1987;vol. 2:856–60.
[21] Telesman J, Gabb TP, Yamada Y, Drapper SL. Fatigue resistance of a hot corrosion exposed disk superalloy at varied test temperatures. Mater High Temp 2016;33(4–5):517–27. https://doi.org/10.1080/09603409.2016.1179000.
[22] Hudak Jr. SJ, Chan KS, Chell GG, Lee Y-D, McClung RC. Proceedings of David L. Davidson symposium on fatigue. Warrendale, PA: TMS; 2002. p. 107–20.
[23] El Haddad MH, Smith KN, Topper TH. Fatigue crack propagation of short cracks. ASME J Eng Mater Tech 1979;101:42–6.
[24] Chan KS. Roles of microstructure in fatigue crack initiation. Int J Fatigue 2010;32:1428–47.
[25] Gabb TP, Garg A, Ellis DL, O'Connor KM. Detailed Microstructural Characterization of the Disk Alloy ME3. NASA/TM-2004-213066. Cleveland, OH: NASA Glenn Research Center; 2004.
[26] Chan KS, Enright MP, Moody JP, Fitch SHK. A Microstructure-based time-dependent crack growth model for life and reliability prediction of turbopropulsion systems. Metallurgical and Materials Transactions A 2014;45A:287–301. https://doi.org/10.1007/s11661-013-1971-9.